ACS APPLIED MATERIALS & INTERFACES

www.acsami.org

Research Article

Ferroelectric Tunable Nonvolatile Polarization Detection Based on 2H α-In_2Se_3

Tengzhang Liu,[¶] Xin Huang,*[,¶] Zhuoxuan Han, Qinghu Bai, Yang Guo, Han Chen, Lin Wang, Cai Luo, Baogang Quan, Haifang Yang, Weiying Zheng, Zhiquan Liu, Baoli Liu, Wugang Liao,* and Changzhi Gu*

Cite This: *ACS Appl. Mater. Interfaces* 2025, 17, 18592−18600

Read Online

ACCESS | Metrics & More | Article Recommendations | Supporting Information

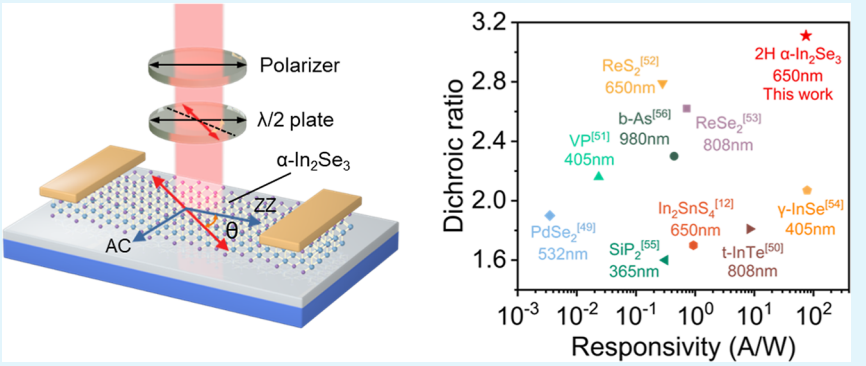

ABSTRACT: The development of polarization photodetectors utilizing two-dimensional materials holds significant promise due to their distinctive properties and potential for high integration. However, a major limitation of most current polarization photodetectors is their lack of polarization tuning capability, which restricts the versatility of individual devices. In this study, a nonvolatile ferroelectric tunable polarization photodetector is explored based on 2H α-In_2Se_3. The ferroelectric semiconductor field-effect transistor (FeS-FET) based on 2H α-In_2Se_3 were fabricated, demonstrating an on/off ratio of 10^3. Ferroelectric modulation photoelectric response was explored under 650 nm illumination, the device achieves a maximum optical responsivity of 75 A/W, with a detectivity of 1.46×10^{10} jones. Notably, in the context of polarized light detection, the device's polarization sensitivity experiences significant modulation due to ferroelectric polarization switching. The dichroic ratios can be tuned to 1.74 and 3 for polarization down and up states, respectively. Moreover, by adjusting the degree of ferroelectric polarization switching, the dichroic ratio can be linearly tuned. The polarization up state can continuously enhance the dichroic ratio in the range of 2.71−3.11, while the polarization down state can continuously weaken the dichroic ratio in the range of 2.54−2.06. This research not only advances the understanding of 2H α-In_2Se_3 in polarization detection but also introduces a nonvolatile ferroelectric modulation approach for tunable polarization detection.

KEYWORDS: *ferroelectricity, polarization detection, tunable, 2D materials, indium selenides*

1. INTRODUCTION

Polarization-sensitive photodetectors have garnered significant attention due to their crucial roles in various fields such as remote sensing, navigation, and biomedical diagnostics.[1−5] Traditional polarization photodetectors require the integration of polarizers to achieve polarization-sensitive light detection, which increases the size, cost, and complexity.[6] Therefore, it is crucial to develop all-in-one micro- and nanoscale polarization photodetectors.[7] In recent years, two-dimensional (2D) semiconductor materials with in-plane anisotropic low-symmetry lattice structures gained wide attention in polarization-sensitive optoelectronics due to their unique physical properties, atomically smooth surfaces without dangling bonds, and their potential compatibility with CMOS processes.[8−11]

However, the 2D material-based polarization photodetectors are severely limited in diverse applications due to the lack of effective strategies for tuning the response to polarized light.[12] Although there has been research on tunable polarization photodetectors, several issues still impede their further development.[13] For instance, Zuo et al. fabricated an In_2SnS_4-based polarization photodetector, achieving modula-

Received: December 14, 2024
Revised: February 25, 2025
Accepted: March 4, 2025
Published: March 6, 2025

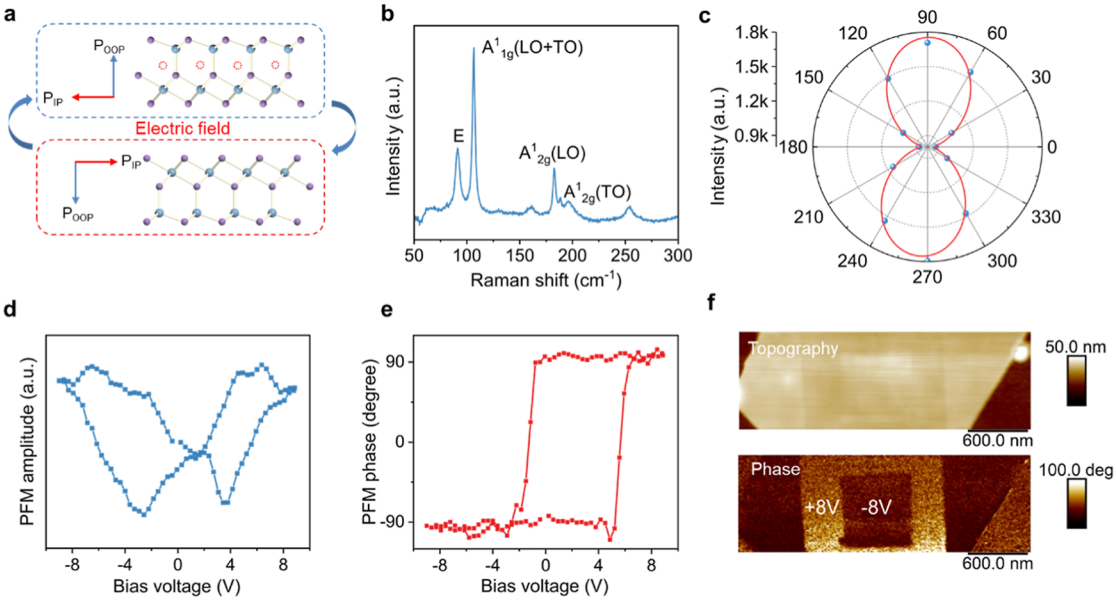

Figure 1. PFM and Raman spectroscopy characteristics of 2H α-In_2Se_3. (a) Side view of the monolayer 2H α-In_2Se_3. Red and blue arrows represent IP and OOP ferroelectric polarization directions, respectively. The red dashed circles indicate the corresponding displacement of Se atoms in the central layer during polarization switching under an external electric field. (b) Raman spectrum of 2H α-In_2Se_3. (c) Polar plot of the Raman peak intensity of the A_{1g}^1 mode as a function of rotation angle of incident polarized light, with blue dots representing experimental data points and the red curve representing the fitted curve. (d) PFM amplitude and (e) phase hysteresis loop of a 2H α-In_2Se_3 flake with a thickness of 52.4 nm. (f) Domain pattern writing. The top half shows the topography of 2H α-In_2Se_3 with a thickness of 20.4 nm. The bottom half is a box-in-box phase image. The inner and outer square areas respectively apply −8 and +8 V voltage to write the downward and upward ferroelectric domains.

tion of the dichroic ratio in the range of 1.13 to 1.70 by applying a back-gate voltage to adjust the metal−semiconductor contact barrier.[12] However, this approach requires sustained external gate voltage, which is unfavorable for low-power applications. In addition, Shen et al. constructed a Gr/2H-$MoTe_2$/BP vertical heterojunction that demonstrated 2 orders of magnitude anisotropic modulation in the telecommunication band by adjusting the gate voltage to work within different spectral response ranges.[14] Although constructing a heterojunction effectively improves anisotropy and tunability,[13,15,16] it adds complexity to the device structure and fabrication difficulty.[8,17,18] Ferroelectric tuning polarization detection is a highly promising strategy due to its nonvolatility, which reduces the power consumption of device. Wu et al. induced rotational symmetry breaking in $MoTe_2$ by defining noncentrosymmetric T-shaped ferroelectric domain patterns on P(VDF-TrFE) to achieve polarization light detection.[19] And the optimal polarized light detection under the bulk photovoltaic effect can be achieved by carefully designing the ferroelectric domain pattern. Although ferroelectric domain engineering has achieved excellent ferroelectric tunability and polarization detection performance, the definition of specific ferroelectric domain patterns remains challenging. Additionally, the low domain writing efficiency hinders the configuration of device. Furthermore, current ferroelectric tuning strategies primarily involve external influences, and the relationship between the ferroelectricity of the material itself and the polarization response remains underexplored.

Therefore, there is an urgent need to develop a ferroelectric tunable polarization photodetector that is simple, easily fabricated, and more feasible for practical implementation. The 2H α-In_2Se_3 from the ferroelectric material family is a promising candidate for exploration. It is a stable 2D layered ferroelectric semiconductor with out-of-plane (OOP) and in-plane (IP) polarization dipole locking and excellent optoelectronic performance, has garnered significant research interest.[20−22] Moreover, the noncentrosymmetric lattice structure of 2H α-In_2Se_3 gives it in-plane anisotropy, making it suitable for polarization light detection.[23] Therefore, leveraging the ferroelectricity in 2H α-In_2Se_3 to modulate its polarization sensitivity represents a novel approach for ferroelectric tunable polarization photodetectors.

In this work, we effectively tuned the dichroic ratio of a 2H α-In_2Se_3-based device by switching its ferroelectric polarization. First, the anisotropic crystal structure and ferroelectricity of the material were confirmed through polarization Raman spectroscopy and piezoresponse force microscopy (PFM) measurements. Subsequently, the electrical performance of a 2H α-In_2Se_3-based semiconductor field-effect transistor was tested. The device exhibited excellent memory performance, with an on/off ratio greater than 10^3 and nonvolatile ferroelectric tunable conductivity. The responsivity of the device also showed ferroelectric tunability. Under 650 nm laser illumination, the maximum responsivity reached 75 A/W, and the maximum specific detectivity reached 1.46×10^{10} jones. The mechanism by which the ferroelectric polarization modulates the photocurrent under illumination was also discussed in detail. Finally, a large, continuously linear tunable dichroic ratio was achieved by gradually switching ferroelectric polarization. In the upward polarization state, the dichroic ratio could be tuned from 2.71 to 3.11, while in the downward polarization state, it ranged from 2.54 to 2.06. The device demonstrated outstanding polarization sensitivity and nonvolatile tunability. These findings not only advance the research on α-In_2Se_3 in polarization photodetection, but also provide a more efficient and flexible ferroelectric tuning method for polarization photodetectors.

https://doi.org/10.1021/acsami.4c21713
ACS Appl. Mater. Interfaces 2025, 17, 18592−18600

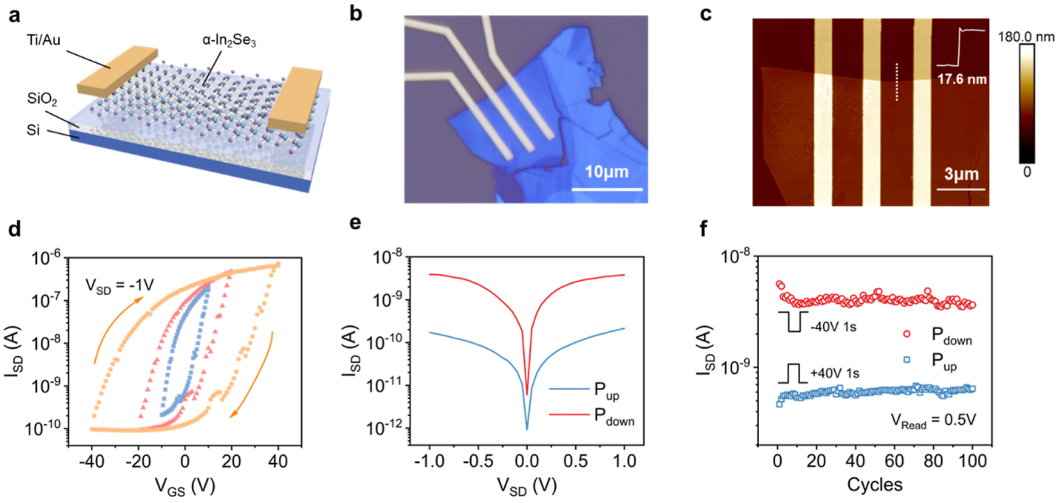

Figure 2. Schematic and electrical characteristics of the 2H α-In_2Se_3 FeS-FET. (a) 3D schematic of the FeS-FET. (b) Optical microscope image of the device. (c) AFM topography of the device and the thickness of the nanosheet along the white dashed line are approximately 17.6 nm. (d) Transfer characteristic curve of the device at V_{SD} = −1 V. (e) Output characteristic curves of the device in the P_{up} state (+40 V gate voltage pulse) and P_{down} state (−40 V gate voltage pulse). (f) Cycling test for the P_{up} and P_{down} states.

2. RESULTS AND DISCUSSION

2.1. Material Properties. The ferroelectricity and anisotropy of 2H α-In_2Se_3 are closely linked to its crystal structure. Figure 1a shows the side view of the 2H α-In_2Se_3 crystal. It is composed of quintuple layers of Se−In−Se−In−Se, stacked in a layered structure.[24] Within each quintuple layer, two In atoms bond with adjacent Se atoms in octahedral and tetrahedral configurations, respectively. The Se atom in the central of the quintuple layer forms a kink with two differently coordinated In atoms, resulting in a noncentrosymmetric crystal structure.[25] This structural asymmetry leads to the strong ferroelectricity and anisotropy.[25,26] The ferroelectricity can be switched under an external electric field, which is caused by the slanted migration of the central layer Se atoms,[27] as indicated by the red dashed circle in Figure 1a, accompanied by coupled polarization switching both IP and OOP.[28]

Raman spectroscopy of the material is shown in Figure 1b, four characteristic peaks are observed at 90, 106, 183, and 196 cm^{-1}, corresponding to E, A_{1g}^1 (LO + TO), A_{2g}^1 (LO), and A_{2g}^1 (TO) phonon modes, respectively.[29] The peak at 90 cm^{-1} verifies the 2H polytype,[30] while the peak at 106 cm^{-1} indicates that the material is the α phase.[25] Angle-resolved polarized Raman spectroscopy was collected at different incident light polarization angles, as shown in Figure S1. According to the classical Raman selection rule, the Raman scattering intensity I of 2H α-In_2Se_3 can be expressed as[23,31]

$$I \propto (a\cos^2\theta + b\sin^2\theta)^2 \quad (1)$$

where θ is the rotation angle of the incident polarized light. As shown in Figure 1c, the experimental data are well fitted by this expression. The intensity of the A_{1g}^1 peak exhibits a 180° periodic variation with respect to the polarization angle of the incident light, with an anisotropy ratio of 2.03, indicating strong anisotropic phonon vibrations in the crystal.

Figure 1d,e are the out-of-plane PFM amplitude and phase hysteresis loops of a 2H α-In_2Se_3 flake with a thickness of 52.4 nm, respectively. The butterfly shaped amplitude hysteresis loop and the 180° phase reversal confirm the ferroelectricity of 2H α-In_2Se_3,[32] with a coercive electric field for the out-of-plane ferroelectric polarization switching of approximately 600 kV cm^{-1}. To verify the nonvolatility of the ferroelectric polarization, a conductive atomic force microscopy (AFM) probe was used to write ferroelectric domains with opposite polarization directions in different size areas on a 20.4 nm thick 2H α-In_2Se_3 flake. The probe was first biased at +8 V to scan an area of 1.5 × 1.5 μm^2, and then scanned a smaller area of 1 × 1 μm^2 at −8 V. Consequently, the local ferroelectric polarization within the defined areas exhibited an upward state within the frame and a downward state outside the frame under the influence of the external electric field, forming the box-in-box PFM phase image as shown in Figure 1f. Moreover, there was no significant damage to the morphology of the corresponding areas.

2.2. Device Structure and Electrical Characteristics. By using mechanical exfoliation, 2H α-In_2Se_3 nanosheets were successfully obtained from bulk materials and transferred onto SiO_2 (285 nm)/Si substrate. Source−drain electrodes, consisting of 30 nm Ti/40 nm Au, were patterned via electron beam lithography and deposited via electron beam evaporation, resulting in the fabrication of 2H α-In_2Se_3-based FeS-FET. Figure 2a,b show the 3D schematic and optical microscope image of the device, respectively. The AFM topography of the device is shown in Figure 2c, where the thickness of the α-In_2Se_3 nanosheet is measured to be approximately 17.6 nm, as measured along the white dashed line. The optical microscope image and AFM morphology showed that the nanosheet in the channel region had no wrinkles and bubbles, exhibiting good uniformity.

The transfer characteristics of the device at V_{SD} = −1 V are depicted in Figure 2d, showing typical n-type doping behavior. The cyclic scanning reveals a pronounced clockwise hysteresis phenomenon, with an on/off ratio greater than 10^3 (V_{GS} = 0 V) and a memory window of about 60 V (I_{SD} = 8.5 × 10^{-9} A), occupying 75% of the entire scan range. The large on/off ratio and memory window indicate excellent memory performance of our device. Moreover, this excellent performance can be reproduced in five similar devices, as shown in Figure S2. To investigate the main causes of the large hysteresis observed in the transfer curve, a detailed discussion is provided in Figure S3. Several factors may contribute to the hysteresis

https://doi.org/10.1021/acsami.4c21713
ACS Appl. Mater. Interfaces 2025, 17, 18592−18600

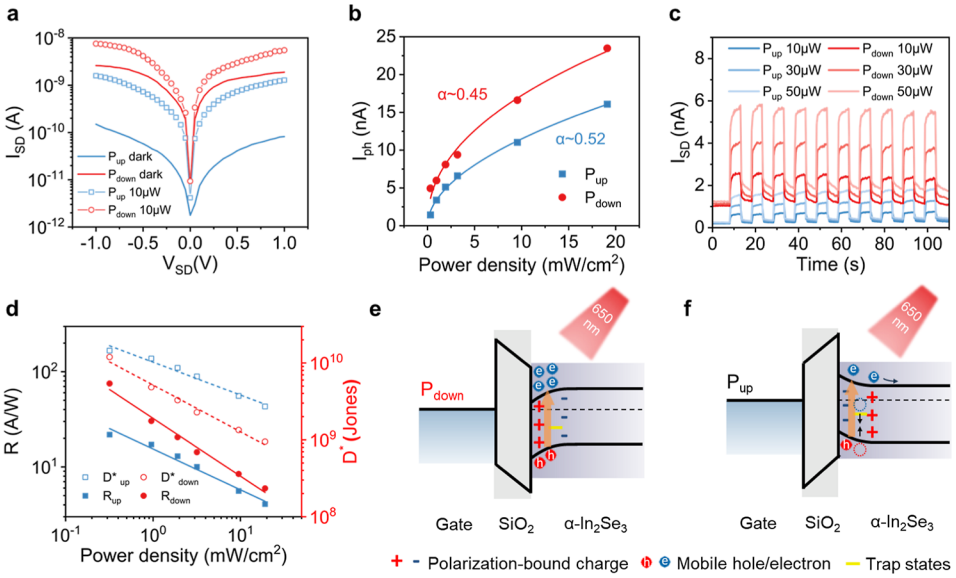

Figure 3. Photoresponse characteristics and working mechanism of the 2H α-In_2Se_3 FeS-FET. (a) Output characteristic curves of the device in the P_{up} and P_{down} states under dark conditions and 650 nm light illumination at 0.32 mW/cm^2. (b) Power-dependent photocurrent at V_{SD} = −1 V. (c) Time-resolved photoresponse in the P_{up}/P_{down} states at V_{SD} = −0.5 V. (d) Responsivity and specific detectivity of the two polarization states at V_{SD} = −1 V. Energy band diagrams for the (e) P_{down} and (f) P_{up} states under illuminated. The orange arrow signifies the excitation process of photogenerated charge carriers under illumination.

phenomenon, including the ferroelectric polarization, interface and bulk trap states, water and oxygen molecules in the air, etc. Under the same structure and test conditions, the comparative MoS_2-FET exhibits a negligible hysteresis, suggesting that the contributions of interface defects, water molecules, and oxygen molecules in the air to the hysteresis can be ignored. Moreover, the α-In_2Se_3 FeS-FET still shows large hysteresis under high vacuum conditions, ruling out the effect of water and oxygen molecules. The above suggest that the significant cyclic hysteresis observed in Figure 1d is primarily caused by the nonvolatile ferroelectric polarization switching in α-In_2Se_3, which has also been confirmed in many related studies.[33−35] The clockwise hysteresis indicates that the switching occurs only partially near the oxide−semiconductor interface, leading to variations in carrier concentration in the channel and consequently low and high resistance states during forward and reverse scans, respectively.[33,36] Figure 1e illustrates the output characteristic curves of the device at different ferroelectric polarization states at V_{GS} = 0 V. By applying positive gate pulses of 40 V and negative gate pulses of −40 V, the device is respectively set into the polarization-up (P_{up}) and polarization-down (P_{down}) states. The results reveal a significant modulation effect of nonvolatile ferroelectric polarization on the device's conductivity, with an on/off ratio exceeding an order of magnitude. To demonstrate the cyclic stability of the device under sufficient ferroelectric polarization switching, the endurance of the device was tested under pulse cycles of ±40 V 1 s. As shown in Figure 2f, the device exhibits stable ferroelectric polarization switching, maintaining performance for over 10^2 cycles.

2.3. Photoresponse Characteristics and Working Mechanism. With a suitable bandgap of approximately 1.41 eV (as shown in Figure S4), α-In_2Se_3 is well-suited for photodetection in the visible to near-infrared range. The optical response characteristics of the device were tested under 650 nm laser illumination. Figure 3a presents the output characteristic curves of the device in both darkness and under illumination. The results clearly show that both dark current and photocurrent can be significantly modulated by switching the ferroelectric polarization. At a power density of 0.32 mW/cm^2, the photocurrent in the P_{down} state is nearly four times greater than that in the P_{up} state. As shown in Figure 3b, the photocurrent exhibits a nearly linear relationship with optical power at V_{SD} = −1 V. The power-law relationship between photocurrent and optical power is given by $I_{ph} = B{\cdot}P^{\alpha}$, where I_{ph} is the photocurrent given by $I_{light} - I_{dark}$, B is a constant, P is the optical power, and α is the fitting parameter representing the linearity of the photodetector.[37] In the P_{up} and P_{down} states, α is 0.52 and 0.45, respectively. The value of α being far below 1 indicates the presence of numerous trap states in the device, leading to frequent recombination. These trap states may be due to water molecules absorption in the air and Se vacancies within the material.[38,39]

To assess the stability and reproducibility of the device across different ferroelectric polarization states, the time-resolved optical response switching behavior was tested at various power levels, as illustrated in Figure 3c. Under a V_{SD} = −0.5 V bias, the device demonstrated stable switching behavior over ten consecutive light-on and light-off cycles, with good recognition to different optical power levels. A slight degradation observed in the P_{down} state is attributed to a minor depolarization effect; however, the device demonstrated relatively good stability and repeatability within the test duration. Although photoinduced ferroelectric polarization switching exists in many ferroelectric materials, its occurrence requires certain conditions, including wavelength, power, irradiation time, and the environment.[40−42] Under our test condition, it is not able to meet the requirements to trigger the possible polarization switching.

The responsivity (R) and specific detectivity (D^*) are key metrics for evaluating photodetectors and can be calculated using the following expressions

https://doi.org/10.1021/acsami.4c21713
ACS Appl. Mater. Interfaces 2025, 17, 18592−18600

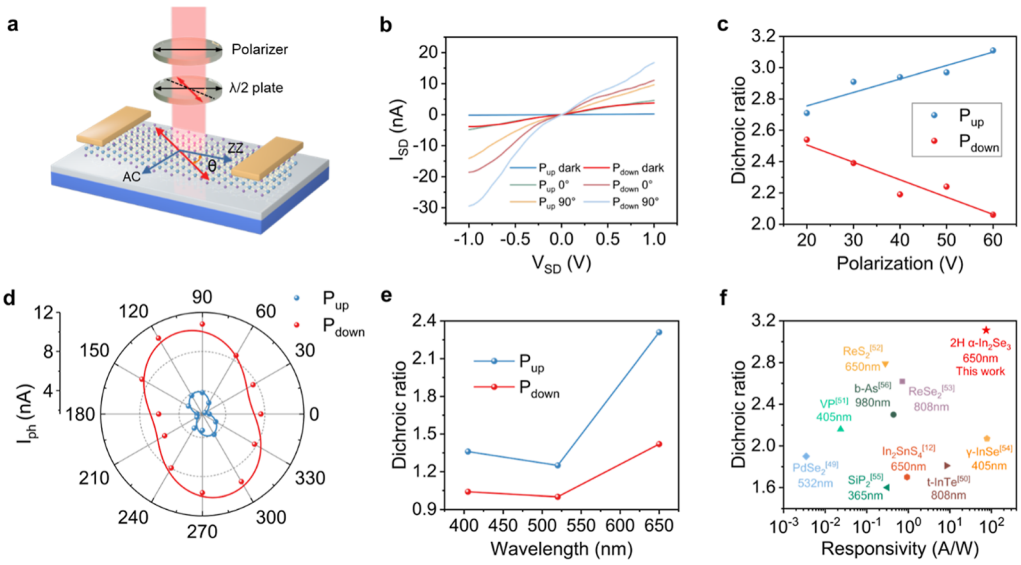

Figure 4. Ferroelectric-tunable polarization photoresponse characteristics. (a) Schematic of the linearly polarized light detection using the 2H α-In_2Se_3-based photodetector. θ represents the angle between the polarization direction of the incident light and the zigzag (ZZ) orientation of the crystal. When θ = 90°, the polarization direction of the incident light aligns with the armchair (AC) direction of the crystal. (b) Output characteristic curves in the P_{up}/P_{down} states under dark conditions and under 650 nm polarized light illumination at 1.91 mW/cm^2 with θ = 0° and 90°. (c) Dichroic ratio as a function of different degrees of ferroelectric polarization switching (at V_{SD} = −1 V). (d) Polar plot of the angle-resolved photocurrent as a function of polarization angle at V_{SD} = −0.5 V. (e) Dichroic ratio under illumination of different wavelengths (at V_{SD} = −0.5 V). (f) Comparison of the dichroic ratio and responsivity performance of 2D material-based polarized photodetectors with similar structures.

$$R = \frac{I_{ph}}{P \times S} \tag{2}$$

$$D^* = \frac{R \times A^{1/2}}{(2eI_{dark})^{1/2}} \tag{3}$$

where S is the effective channel excitation area, A is the effective area of the device, e is the electron charge, and I_{dark} is the dark current. Figure 3d shows the calculated R and D^* for the device at V_{SD} = −1 V under both polarization states. There is a clear modulation of responsivity and specific detectivity due to the ferroelectric polarization switching. The responsivity in the P_{down} state is higher than that in the P_{up} state, while the specific detectivity shows the opposite trend. This phenomenon is due to the higher noise current in the P_{down} state, whereas in the P_{up} state, the depletion of majority carrier electrons effectively reduces the noise current.[43,44] Therefore, the increase in responsivity in the P_{down} state is offset by the larger noise current, leading to a decrease in specific detectivity. The enhanced responsivity in the P_{down} state is associated with ferroelectric polarization and trap states, which will be discussed in detail later. At a power density of 0.32 mW/cm^2, the device achieves a maximum responsivity of 75 A/W in the P_{down} state, and a maximum specific detectivity of 1.46 × 10^{10} jones in the P_{up} state. Additionally, we calculated the device's external quantum efficiency (EQE). As shown in Figure S5, where the maximum values in the P_{up} and P_{down} states are 4171% and 14,357%, respectively. For another 2H α-In_2Se_3 device, excellent performance and similar ferroelectric modulation effect has also been achieved, as shown in Figure S6. These parameters highlight the excellent optoelectronic properties of 2H α-In_2Se_3. Notably, both the responsivity and EQE exceed that of most 2D material-based photodetectors. Furthermore, the introduction of ferroelectric tunability enhances the flexibility of the device.

Moreover, the underlying mechanism of the modulation effect has been further discussed. As can be seen from the above results, a significant difference in photocurrent is observed between the P_{up} and P_{down} states. Specifically, the photocurrent is higher in the P_{down} state compared to the P_{up} state. To elucidate this phenomenon, it is necessary to consider both ferroelectric polarization and trap states comprehensively. As shown in Figure 3e, the negative gate voltage pulse switches the ferroelectric polarization to the P_{down} state, and photogenerated carriers are separated under the applied electric field, resulting in photocurrent. Ferroelectric polarization further enhances the accumulation of photogenerated electrons in the channel, while the repulsion of electrons during negative pulses leaves the trap states unoccupied. Hence, the photocurrent is elevated in this state. Conversely, as shown in Figure 3f, in the P_{up} state, the photogenerated electrons are driven away from the channel by the ferroelectric polarization, and the electrons trapped by positive pulses recombine with photogenerated holes.[33,39] This further reduces the concentration of accumulated photogenerated holes in the channel, leading to a lower photocurrent. Therefore, under illumination, the primary role of ferroelectric polarization is to regulate the dominant type of photogenerated carriers in the channel, while the presence of trap states plays a dominant role in controlling the overall level of photocurrent.

2.4. Ferroelectric-Tunable Polarization Photoresponse. The inherent anisotropy of 2H α-In_2Se_3 makes it a promising candidate for polarization-sensitive photodetection. To explore this potential, the polarization photodetection capabilities of the device were examined. As depicted in the schematic of Figure 4a, a polarizer and a half-wave (λ/2) plate were inserted before the incident light reached the sample. The laser was converted into linearly polarized light using the polarizer, and the λ/2 plate was used to adjust the polarization angle of the incident light without affecting the laser's power. We define θ as the angle between the polarization direction of

https://doi.org/10.1021/acsami.4c21713
ACS Appl. Mater. Interfaces 2025, 17, 18592−18600

the incident light and the zigzag direction of the crystal. Figure 4b shows the output characteristics of the device under polarized light at different θ and ferroelectric polarization states. Positive and negative gate voltage pulses of 50 V were applied to set the device into the P_{up} and P_{down} states, respectively. At $\theta = 0°$, the photocurrent is minimal, while at $\theta = 90°$, the photocurrent is maximal. The dichroic ratios (DR = I_{phmax}/I_{phmin}) under P_{up} and P_{down} states are 3 and 1.74 at $V_{SD} = -1$ V, respectively, clearly demonstrating the modulation of the DR by ferroelectric polarization switching. Three possible reasons for this pronounced modulation effect have been proposed. First, the lattice anisotropy would be modulated by ferroelectric polarization, which is verified by the polarization-resolved Raman spectroscopy under different ferroelectric polarization states, as shown in Figure S7. Second, the anisotropic carrier transport can be modulated by the ferroelectric polarization and the increased carrier concentration in the P_{down} state may suppress the contribution from anisotropic transport.[23] Third, the anisotropic light absorption would be modulated by the ferroelectric polarization.[45] However, the latter two possibilities require further theoretical and experimental investigation for validation.

To further explore the modulation effect of ferroelectricity on polarization sensitivity, the DR at different degree of ferroelectric polarization was studied. As shown in Figure 4c, by applying gate voltage pulses with a gradually increasing amplitude, the ferroelectric polarization of the device was gradually switched. The photocurrents at $\theta = 0°$ and $\theta = 90°$ were then measured, as shown in Figure S8. The extracted DR exhibited a linear dependence on the voltage amplitude. As the amplitude increased, the DR in P_{up} state rises from 2.71 to 3.11, while the DR in P_{down} state decreases from 2.54 to 2.06, demonstrating a continuous potentiation and depression behaviors of DR. Furthermore, similar ferroelectric modulation effects have also been observed in another similar device, as shown in Figure S9. The linear modulation behavior of DR is analogous to the application of α-In_2Se_3 in neuromorphic simulations, where ferroelectric polarization can be gradually switched by applying an appropriate pulse sequence, leading to a linear modulation of the device's conductivity state and enabling in-memory computing.[46,47] The linear modulation of DR provides a new degree of freedom for neuromorphic simulation, which could potentially be used to construct polarization-sensitive neuromorphic systems.

The angle-resolved photocurrents in two different polarization states are plotted as functions of the polarization angle θ in the polar coordinate system shown in Figure 4d, and the corresponding optical switching curves are shown in Figure S10b,e. The relationship between the photocurrent and the polarization angle can be fitted using the following equation[48]

$$I(\theta) = I_{phmin}\sin^2(\theta) + I_{phmax}\cos^2(\theta) \quad (4)$$

It is evident that the photocurrent exhibits a periodic variation of 180° with the changes of polarization angle, demonstrating the nonvolatility and stability of our device. In addition, at a laser power density of 0.95 and 3.2 mW/cm^2 (1.91 mW/cm^2 in Figure 4d), the device also has good polarization sensitivity, see Figures S10 and S11. Additionally, the device's DR was also tested at various wavelengths. As shown in Figures 4e and S12, the device exhibits the strongest polarization response under 650 nm laser. Figure 4f provides a comparison of the responsivity and dichroic ratio of several 2D material-based polarization photodetectors with similar structures reported in recent years.[12,49−56] The 2H α-In_2Se_3-based phototransistor in this work demonstrates a higher dichroic ratio, along with considerable responsivity, positioning it as a highly competitive among 2D material-based polarization photodetectors.

3. CONCLUSION

In summary, we have developed a polarization photodetector based on 2H α-In_2Se_3, achieving nonvolatile ferroelectric tunability for polarization detection. By modulating the ferroelectric polarization states, we successfully tuned the conductivity, responsivity, and dichroic ratio. For the first time, the modulation of polarization detection by the ferroelectricity of the ferroelectric material itself was investigated in our device. The device reached a maximum dichroic ratio of 3.11, demonstrating excellent polarization detection capabilities. Furthermore, the continuous and linear tunability of the dichroic ratio introduces a new degree of freedom in the field of tunable devices, opening up possibilities for a wide range of potential applications, such as polarization-sensitive neuromorphic systems, polarization sensing−computing devices, and polarization encryption, etc. This work extends the research of 2H α-In_2Se_3 in the field of polarization detection and proposes a more efficient and flexible ferroelectric tuning method for tunable polarization detection.

4. EXPERIMENTAL SECTION

4.1. Device Fabrication. Multilayer α-In_2Se_3 nanosheets were mechanically exfoliated from bulk material (purchased from HQ Graphene) using transparent tape, and then transferred to a 285 nm SiO_2/Si substrate with polydimethylsiloxane (PDMS). 495A5 PMMA photoresist was applied to define the electrode pattern via electron beam lithography (Raith 150). Thirty nm Ti/40 nm Au electrode was deposited using electron beam evaporation (Peva-600E) in a high vacuum ($<5 \times 10^{-7}$ Torr) and subsequently subjected to a standard lift-off process in acetone. The devices were annealed at 180 °C for 1 h under high vacuum ($<3 \times 10^{-4}$ Torr) to eliminate surface bubbles and improve contact quality.

4.2. Device Characterization. The device morphology was characterized using optical microscopy (MX50), while the thickness of the nanosheets was determined with atomic force microscopy (Bruker Dimension Icon). The ferroelectricity was verified by piezoresponse force microscopy (Asylum Research MFP-3D AFM). Raman spectra and angle-resolved polarized Raman spectra (ARPRS) were collected by Raman spectrometer (LabRAM HR Evolution NANO) under 633 nm laser excitation. For the ARPRS tests, the configuration involved fixing the sample and varying the polarization direction of the incident light.

4.3. Photoelectric Measurements. The electrical and photoelectric characteristics of the devices were measured using a probe station and a semiconductor analyzer (4200SCS, Keithley). The photoelectric measurements were conducted on a self-built optical platform. The angle-resolved photocurrent was measured using a half-wave plate and a polarizer, with the laser polarization direction determined by the polarizer and modulated to achieve linearly polarized light. The polarization angle of the incident light was adjusted by rotating the half-wave plate without affecting the laser power.

■ ASSOCIATED CONTENT

Supporting Information

The Supporting Information is available free of charge at https://pubs.acs.org/doi/10.1021/acsami.4c21713.

Polarization Raman spectra of 2H α-In_2Se_3; photoluminescence (PL) spectra of 2H α-In_2Se_3; switching

https://doi.org/10.1021/acsami.4c21713
ACS Appl. Mater. Interfaces 2025, 17, 18592−18600

curves of 2H α-In_2Se_3 based FeS-FET; polar plots of angle-resolved photocurrent; output characteristic curves with different degrees of ferroelectric switching under illumination at different polarization angles; the electrical characteristics and ferroelectrically tunable polarization detection of another similar device; polarization response with 405 and 520 nm lasers (PDF)

AUTHOR INFORMATION

Corresponding Authors

Xin Huang − *Beijing National Laboratory for Condensed Matter Physics, Institute of Physics, Chinese Academy of Sciences, Beijing 100190, People's Republic of China; School of Physical Sciences, CAS Key Laboratory of Vacuum Physics, University of Chinese Academy of Sciences, Beijing 100190, People's Republic of China*; Email: xinhuang@iphy.ac.cn

Wugang Liao − *State Key Laboratory of Radio Frequency Heterogeneous Integration, College of Electronics and Information Engineering, Shenzhen University, Shenzhen 518060, China*; orcid.org/0000-0002-1461-2222; Email: wgliao@szu.edu.cn

Changzhi Gu − *Beijing National Laboratory for Condensed Matter Physics, Institute of Physics, Chinese Academy of Sciences, Beijing 100190, People's Republic of China; School of Physical Sciences, CAS Key Laboratory of Vacuum Physics, University of Chinese Academy of Sciences, Beijing 100190, People's Republic of China*; orcid.org/0000-0002-2689-2807; Email: czgu@iphy.ac.cn

Authors

Tengzhang Liu − *State Key Laboratory of Radio Frequency Heterogeneous Integration, College of Electronics and Information Engineering, Shenzhen University, Shenzhen 518060, China; Beijing National Laboratory for Condensed Matter Physics, Institute of Physics, Chinese Academy of Sciences, Beijing 100190, People's Republic of China*

Zhuoxuan Han − *Beijing National Laboratory for Condensed Matter Physics, Institute of Physics, Chinese Academy of Sciences, Beijing 100190, People's Republic of China*

Qinghu Bai − *Beijing National Laboratory for Condensed Matter Physics, Institute of Physics, Chinese Academy of Sciences, Beijing 100190, People's Republic of China; School of Physical Sciences, CAS Key Laboratory of Vacuum Physics, University of Chinese Academy of Sciences, Beijing 100190, People's Republic of China*

Yang Guo − *Beijing National Laboratory for Condensed Matter Physics, Institute of Physics, Chinese Academy of Sciences, Beijing 100190, People's Republic of China; School of Physical Sciences, CAS Key Laboratory of Vacuum Physics, University of Chinese Academy of Sciences, Beijing 100190, People's Republic of China*; orcid.org/0000-0001-8975-9387

Han Chen − *School of Mechanical Engineering, Shanghai Jiao Tong University, Shanghai 200240, China*

Lin Wang − *School of Mechanical Engineering, Shanghai Jiao Tong University, Shanghai 200240, China*; orcid.org/0000-0003-3430-7345

Cai Luo − *Beijing National Laboratory for Condensed Matter Physics, Institute of Physics, Chinese Academy of Sciences, Beijing 100190, People's Republic of China*

Baogang Quan − *Beijing National Laboratory for Condensed Matter Physics, Institute of Physics, Chinese Academy of Sciences, Beijing 100190, People's Republic of China*

Haifang Yang − *Beijing National Laboratory for Condensed Matter Physics, Institute of Physics, Chinese Academy of Sciences, Beijing 100190, People's Republic of China*

Weiying Zheng − *State Key Laboratory of Radio Frequency Heterogeneous Integration, College of Electronics and Information Engineering, Shenzhen University, Shenzhen 518060, China*

Zhiquan Liu − *State Key Laboratory of Radio Frequency Heterogeneous Integration, College of Electronics and Information Engineering, Shenzhen University, Shenzhen 518060, China*

Baoli Liu − *Beijing National Laboratory for Condensed Matter Physics, Institute of Physics, Chinese Academy of Sciences, Beijing 100190, People's Republic of China; Songshan Lake Materials Laboratory, Dongguan 523808, People's Republic of China; CAS Center for Excellence in Topological Quantum Computation, CAS Key Laboratory of Vacuum Physics, University of Chinese Academy of Sciences, Beijing 100190, People's Republic of China*

Complete contact information is available at: https://pubs.acs.org/10.1021/acsami.4c21713

Author Contributions

¶T.L. and X.H. contributed equally to this work. W. Liao, C.Z. Gu and X. Huang conceived the core ideas and designed the outlines of the manuscript. T.Z. Liu, Z.X. Han and Q.H. Bai fabricated the device. T.Z. Liu and H. Chen conducted the measurements. Q.H. Bai and C. Luo provided assistance for the measurements. T.Z. Liu, X. Huang and W. Liao analyzed the data and drafted the manuscript. W. Liao made significant contributions to revise the manuscript. X. Huang, W. Liao and C.Z. Gu set up the platforms, provided resources, and secured funding for the study. All authors read and approved the submitted version of the manuscript. T.Z. Liu and X. Huang contributed equally to this work.

Notes

The authors declare no competing financial interest.

ACKNOWLEDGMENTS

The work was partially supported by the financial support from the Guangdong Basic and Applied Basic Research Foundation (grant no. 2023A1515010693), partially by the Shenzhen University 2035 Program for Excellent Research (grant no. 2023C008), Shenzhen Science and Technology Program (grant no. ZDSYS20220527171402005), Shenzhen Strategic Emerging Industry Support Plan (grant no. F-2023-Z99-509043), and the National Natural Science Foundation of China (grant nos. 61904110, 62204259, 92265110, 62174179, 52302187). The authors also acknowledge the support from the Instrumental Analysis Center of Shenzhen University (Xili Campus).

REFERENCES

(1) Tyo, J. S.; Goldstein, D. L.; Chenault, D. B.; Shaw, J. A. Review of passive imaging polarimetry for remote sensing applications. *Appl. Opt.* **2006**, *45* (22), 5453−5469.

(2) Powell, S. B.; Garnett, R.; Marshall, J.; Rizk, C.; Gruev, V. Bioinspired polarization vision enables underwater geolocalization. *Sci. Adv.* **2018**, *4* (4), No. eaao6841.

(3) Novikova, T.; Pierangelo, A.; De Martino, A.; Benali, A.; Validire, P. Polarimetric Imaging for Cancer Diagnosis and Staging. *Opt. Photon. News* **2012**, *23* (10), 26−33.

(4) Rubin, N. A.; D'Aversa, G.; Chevalier, P.; Shi, Z.; Chen, W. T.; Capasso, F. Matrix Fourier optics enables a compact full-Stokes polarization camera. *Science* **2019**, *365* (6448), No. eaax1839.
(5) Snik, F.; Julia, C.-J.; Michael, E.; Silvano, F.; David, H.; Antonello De, M.; Dimitri, M.; Jérôme, R.; Tyo, J. S. An overview of polarimetric sensing techniques and technology with applications to different research fields. *Proc. SPIE* **2014**, *9099*, 90990B.
(6) Mohammadi, E.; Behdad, N. A Wide Dynamic Range Polarization Sensing Long Wave Infrared Detector. *Sci. Rep.* **2017**, *7* (1), 17475.
(7) Li, S.; Zhang, J.; Zhu, L.; Zhang, K.; Gao, W.; Li, J.; Huo, N. Reconfigurable and Broadband Polarimetric Photodetector. *Adv. Funct. Mater.* **2023**, *33* (11), 2210268.
(8) Xin, W.; Zhong, W.; Shi, Y.; Shi, Y.; Jing, J.; Xu, T.; Guo, J.; Liu, W.; Li, Y.; Liang, Z.; Xin, X.; Cheng, J.; Hu, W.; Xu, H.; Liu, Y. Low-Dimensional-Materials-Based Photodetectors for Next-Generation Polarized Detection and Imaging. *Adv. Mater.* **2024**, *36* (7), 2306772.
(9) Shen, Y.; Dong, Z.; Sun, Y.; Guo, H.; Wu, F.; Li, X.; Tang, J.; Liu, J.; Wu, X.; Tian, H.; Ren, T. The Trend of 2D Transistors toward Integrated Circuits: Scaling Down and New Mechanisms. *Adv. Mater.* **2022**, *34* (48), 2201916.
(10) Zhang, E.; Wang, P.; Li, Z.; Wang, H.; Song, C.; Huang, C.; Chen, Z.-G.; Yang, L.; Zhang, K.; Lu, S.; Wang, W.; Liu, S.; Fang, H.; Zhou, X.; Yan, H.; Zou, J.; Wan, X.; Zhou, P.; Hu, W.; Xiu, F. Tunable Ambipolar Polarization-Sensitive Photodetectors Based on High-Anisotropy $ReSe_2$ Nanosheets. *ACS Nano* **2016**, *10* (8), 8067−8077.
(11) Kim, K. S.; Kwon, J.; Ryu, H.; Kim, C.; Kim, H.; Lee, E.-K.; Lee, D.; Seo, S.; Han, N. M.; Suh, J. M.; Kim, J.; Song, M.-K.; Lee, S.; Seol, M.; Kim, J. The future of two-dimensional semiconductors beyond Moore's law. *Nat. Nanotechnol.* **2024**, *19* (7), 895−906.
(12) Zuo, N.; Nie, A.; Hu, C.; Shen, W.; Jin, B.; Hu, X.; Liu, Z.; Zhou, X.; Zhai, T. Synergistic Additive-Assisted Growth of 2D Ternary In_2SnS_4 with Giant Gate-Tunable Polarization-Sensitive Photoresponse. *Small* **2021**, *17* (18), 2008078.
(13) Zhang, J.-B.; Zhou, N.; Zhang, L.-H.; Shang, C.-H.; Li, J.-X.; Zhao, Y.; Jia, G.-H.; Yang, R.-S.; Xu, H.; Li, X.-B. Optical and electrical anisotropy regulation engineering of low-dimensional materials toward polarized detection and imaging applications. *Rare Met.* **2024**, *43* (7), 2968−2993.
(14) Shen, D.; Yang, H.; Patel, T.; Rhodes, D. A.; Timusk, T.; Zhou, Y. N.; Kim, N. Y.; Tsen, A. W. Gate-Tunable Multiband van der Waals Photodetector and Polarization Sensor. *ACS Nano* **2024**, *18* (17), 11193−11199.
(15) Wang, J.; Jiang, C.; Li, W.; Xiao, X. Anisotropic Low-Dimensional Materials for Polarization-Sensitive Photodetectors: From Materials to Devices. *Adv. Optical Mater.* **2022**, *10* (6), 2102436.
(16) Wang, H.; Li, Y.; Gao, P.; Wang, J.; Meng, X.; Hu, Y.; Yang, J.; Huang, Z.; Gao, W.; Zheng, Z.; Wei, Z.; Li, J.; Huo, N. Polarization- and Gate-Tunable Optoelectronic Reverse in 2D Semimetal/Semiconductor Photovoltaic Heterostructure. *Adv. Mater.* **2024**, *36* (6), 2309371.
(17) Wang, H.; Li, Z.; Li, D.; Chen, P.; Pi, L.; Zhou, X.; Zhai, T. Van der Waals Integration Based on Two-Dimensional Materials for High-Performance Infrared Photodetectors. *Adv. Funct. Mater.* **2021**, *31* (30), 2103106.
(18) Ahmad, W.; Pan, L.; Khan, K.; Jia, L.; Zhuang, Q.; Wang, Z. Progress and Insight of Van der Waals Heterostructures Containing Interlayer Transition for Near Infrared Photodetectors. *Adv. Funct. Mater.* **2023**, *33* (19), 2300686.
(19) Wu, S.; Deng, J.; Wang, X.; Zhou, J.; Jiao, H.; Zhao, Q.; Lin, T.; Shen, H.; Meng, X.; Chen, Y.; Chu, J.; Wang, J. Polarization photodetectors with configurable polarity transition enabled by programmable ferroelectric-doping patterns. *Nat. Commun.* **2024**, *15* (1), 8743.
(20) Zhang, C.; Zheng, B.; Wu, G.; Liu, X.; Wu, J.; Yao, C.; Wang, Y.; Tang, Z.; Chen, Y.; Fang, L.; Huang, L.; Li, D.; Li, S.; Pan, A. Controlled growth of vertically stacked In_2Se_3/WSe_2 heterostructures for ultrahigh responsivity photodetector. *Nano Res.* **2024**, *17* (3), 1856−1863.
(21) Xiao, J.; Zhu, H.; Wang, Y.; Feng, W.; Hu, Y.; Dasgupta, A.; Han, Y.; Wang, Y.; Muller, D. A.; Martin, L. W.; Hu, P. A.; Zhang, X. Intrinsic Two-Dimensional Ferroelectricity with Dipole Locking. *Phys. Rev. Lett.* **2018**, *120* (22), 227601.
(22) Sun, Y.; Niu, G.; Ren, W.; Meng, X.; Zhao, J.; Luo, W.; Ye, Z.-G.; Xie, Y.-H. Hybrid System Combining Two-Dimensional Materials and Ferroelectrics and Its Application in Photodetection. *ACS Nano* **2021**, *15* (7), 10982−11013.
(23) Wang, S.; Yang, Z.; Wang, D.; Tan, C.; Yang, L.; Wang, Z. Strong Anisotropic Two-Dimensional In_2Se_3 for Light Intensity and Polarization Dual-Mode High-Performance Detection. *ACS Appl. Mater. Interfaces* **2023**, *15* (2), 3357−3364.
(24) Li, J.; Li, H.; Niu, X.; Wang, Z. Low-Dimensional In_2Se_3 Compounds: From Material Preparations to Device Applications. *ACS Nano* **2021**, *15* (12), 18683−18707.
(25) Tan, C. K. Y.; Fu, W.; Loh, K. P. Polymorphism and Ferroelectricity in Indium(III) Selenide. *Chem. Rev.* **2023**, *123* (13), 8701−8717.
(26) Cai, C.; Ling, S.; Hou, P. In-plane anisotropic photoelectric property of α-In_2Se_3 based phototransistor. *Appl. Phys. Lett.* **2023**, *122* (19), 192101.
(27) Wang, X.; Feng, Z.; Cai, J.; Tong, H.; Miao, X. All-van der Waals stacking ferroelectric field-effect transistor based on In_2Se_3 for high-density memory. *Sci. China Inf. Sci.* **2023**, *66* (8), 182401.
(28) Liu, Z.; Hou, P.; Sun, L.; Tsymbal, E. Y.; Jiang, J.; Yang, Q. In-plane ferroelectric tunnel junctions based on 2D α-In_2Se_3/semiconductor heterostructures. *npj Comput. Mater.* **2023**, *9* (1), 6.
(29) Lewandowska, R.; Bacewicz, R.; Filipowicz, J.; Paszkowicz, W. Raman scattering in α-In_2Se_3 crystals. *Mater. Res. Bull.* **2001**, *36* (15), 2577−2583.
(30) Lyu, F.; Li, X.; Tian, J.; Li, Z.; Liu, B.; Chen, Q. Temperature-Driven α-β Phase Transformation and Enhanced Electronic Property of 2H α-In_2Se_3. *ACS Appl. Mater. Interfaces* **2022**, *14* (20), 23637−23644.
(31) Yang, Y.; Liu, S.-C.; Yang, W.; Li, Z.; Wang, Y.; Wang, X.; Zhang, S.; Zhang, Y.; Long, M.; Zhang, G.; Xue, D.-J.; Hu, J.-S.; Wan, L.-J. Air-Stable In-Plane Anisotropic $GeSe_2$ for Highly Polarization-Sensitive Photodetection in Short Wave Region. *J. Am. Chem. Soc.* **2018**, *140* (11), 4150−4156.
(32) Wan, S.; Li, Y.; Li, W.; Mao, X.; Zhu, W.; Zeng, H. Room-temperature ferroelectricity and a switchable diode effect in two-dimensional α-In_2Se_3 thin layers. *Nanoscale* **2018**, *10* (31), 14885−14892.
(33) Si, M.; Saha, A. K.; Gao, S.; Qiu, G.; Qin, J.; Duan, Y.; Jian, J.; Niu, C.; Wang, H.; Wu, W.; Gupta, S. K.; Ye, P. D. A ferroelectric semiconductor field-effect transistor. *Nat. Electron.* **2019**, *2* (12), 580−586.
(34) Wang, L.; Wang, X.; Zhang, Y.; Li, R.; Ma, T.; Leng, K.; Chen, Z.; Abdelwahab, I.; Loh, K. P. Exploring Ferroelectric Switching in α-In_2Se_3 for Neuromorphic Computing. *Adv. Funct. Mater.* **2020**, *30* (45), 2004609.
(35) Chen, Y.; Zhang, M.; Li, D.; Tang, Y.; Ren, H.; Li, J.; Liang, K.; Wang, Y.; Wen, L.; Li, W.; Kong, W.; Liu, S.; Wang, H.; Wang, D.; Zhu, B. Bidirectional Synaptic Phototransistor Based on Two-Dimensional Ferroelectric Semiconductor for Mixed Color Pattern Recognition. *ACS Nano* **2023**, *17* (13), 12499−12509.
(36) Wang, L.; Chen, H.; Chen, M.; Long, Y.; Liu, K.; Loh, K. P. A Scanning Microwave Impedance Microscopy Study of α-In_2Se_3 Ferroelectric Semiconductor. *Adv. Funct. Mater.* **2024**, *34* (28), 2316583.
(37) Jia, C.; Wu, S.; Fan, J.; Luo, C.; Fan, M.; Li, M.; He, L.; Yang, Y.; Zhang, H. Ferroelectrically Modulated and Enhanced Photoresponse in a Self-Powered α-In_2Se_3/Si Heterojunction Photodetector. *ACS Nano* **2023**, *17* (7), 6534−6544.
(38) Zhao, Q.; Wang, W.; Carrascoso-Plana, F.; Jie, W.; Wang, T.; Castellanos-Gomez, A.; Frisenda, R. The role of traps in the

photocurrent generation mechanism in thin InSe photodetectors. *Mater. Horiz.* **2020**, *7* (1), 252−262.
(39) Li, Q.; Yuan, C.; Yu, T.; Wang, Q.; Li, J. Nonvolatile charge memory with optical controllability in two-terminal pristine α-In_2Se_3 nanosheets. *J. Phys. D: Appl. Phys.* **2020**, *53* (7), 075108.
(40) Li, X.; Li, S.; Tian, J.; Lyu, F.; Liao, J.; Chen, Q. Multi-Functional Platform for In-Memory Computing And Sensing Based on 2D Ferroelectric Semiconductor α-In_2Se_3. *Adv. Funct. Mater.* **2024**, *34* (3), 2306486.
(41) Xu, K.; Jiang, W.; Gao, X.; Zhao, Z.; Low, T.; Zhu, W. Optical control of ferroelectric switching and multifunctional devices based on van der Waals ferroelectric semiconductors. *Nanoscale* **2020**, *12* (46), 23488−23496.
(42) Li, T.; Lipatov, A.; Lu, H.; Lee, H.; Lee, J.-W.; Torun, E.; Wirtz, L.; Eom, C.-B.; Íñiguez, J.; Sinitskii, A.; Gruverman, A. Optical control of polarization in ferroelectric heterostructures. *Nat. Commun.* **2018**, *9* (1), 3344.
(43) Kufer, D.; Konstantatos, G. Highly Sensitive, Encapsulated MoS_2 Photodetector with Gate Controllable Gain and Speed. *Nano Lett.* **2015**, *15* (11), 7307−7313.
(44) Yan, T.; Liu, F.; Wang, Y.; Yang, J.; Ding, C.; Cai, Y.; Wu, Z.; Zhan, X.; Wang, F.; Tian, Y.; He, J.; Wang, Z. A Ferroelectric p−i−n Heterostructure for Highly Enhanced Short-Circuit Current Density and Self-Powered Photodetection. *Adv. Electron. Mater.* **2022**, *8* (9), 2101385.
(45) Tang, Z.; Dai, M.; Chen, Y.; He, Q.; Luo, X.; Zheng, Y. Strain Engineering the Ferroelectric Polarization and Optical Absorption in the FEβ-In_2Se_3 Monolayer. *J. Phys. Chem. C* **2022**, *126* (24), 10181−10189.
(46) Guo, F.; Io, W. F.; Dang, Z.; Ding, R.; Pang, S.-Y.; Zhao, Y.; Hao, J. Achieving reinforcement learning in a three-active-terminal neuromorphic device based on a 2D vdW ferroelectric material. *Mater. Horiz.* **2023**, *10* (9), 3719−3728.
(47) Zeng, J.; Feng, G.; Wu, G.; Liu, J.; Zhao, Q.; Wang, H.; Wu, S.; Wang, X.; Chen, Y.; Han, S.; Tian, B.; Duan, C.; Lin, T.; Ge, J.; Shen, H.; Meng, X.; Chu, J.; Wang, J. Multisensory Ferroelectric Semiconductor Synapse for Neuromorphic Computing. *Adv. Funct. Mater.* **2024**, *34* (19), 2313010.
(48) Chen, S.; Ma, J.; Bu, N.; Zheng, T.; Chen, J.; Huang, J.; Luo, X.; Zheng, Z.; Huo, N.; Li, J.; Gao, W. Two-Dimensional GeS/$SnSe_2$ Tunneling Photodiode with Bidirectional Photoresponse and High Polarization Sensitivity. *ACS Appl. Mater. Interfaces* **2024**, *16* (26), 33740−33751.
(49) Zhong, J.; Yu, J.; Cao, L.; Zeng, C.; Ding, J.; Cong, C.; Liu, Z.; Liu, Y. High-performance polarization-sensitive photodetector based on a few-layered $PdSe_2$ nanosheet. *Nano Res.* **2020**, *13* (6), 1780−1786.
(50) Zhou, N.; Dang, Z.; Li, H.; Sun, Z.; Deng, S.; Li, J.; Li, X.; Bai, X.; Xie, Y.; Li, L.; Zhai, T. Low-Symmetry 2D *t*-InTe for Polarization-Sensitive UV-Vis-NIR Photodetection. *Small* **2024**, *20* (40), 2400311.
(51) Chen, W.; Chen, A.; Zhang, R.; Zeng, J.; Zhang, L.; Gu, M.; Wang, C.; Huang, M.; Guo, Y.; Duan, H.; Hu, C.; Shen, W.; Niu, B.; Watanabe, K.; Taniguchi, T.; Zhang, J.; Li, J.; Cai, X.; Liu, G. Strong In-Plane Optoelectronic Anisotropy and Polarization Sensitivity in Low-Symmetry 2D Violet Phosphorus. *Nano Lett.* **2023**, *23* (23), 10821−10831.
(52) Hu, Y.; He, J.; Yan, Z.; Xu, C.; Li, X.; Wei, N.; Wang, Y.; Dong, N.; Wang, J. High Performance Balanced Linear Polarization Photodetector Based on 2D ReS_2. *Laser Photonics Rev.* **2024**, *18*, 2400661.
(53) Song, S.; Zhang, G.; Qiao, J.; Chen, B.; Shen, M.; Yuan, X.; Somekh, M. G.; Feng, F. Highly in-plane anisotropic 2D $ReSe_2$ for polarization-sensitive photodetectors. *Phys. B* **2023**, *663*, 415000.
(54) Pan, Y.; Zhao, Q.; Gao, F.; Dai, M.; Gao, W.; Zheng, T.; Su, S.; Li, J.; Chen, H. Strong In-Plane Optical and Electrical Anisotropies of Multilayered γ-InSe for High-Responsivity Polarization-Sensitive Photodetectors. *ACS Appl. Mater. Interfaces* **2022**, *14* (18), 21383−21391.
(55) Wang, Z.; Luo, P.; Han, B.; Zhang, X.; Zhao, S.; Wang, S.; Chen, X.; Wei, L.; Yang, S.; Zhou, X.; Wang, S.; Tao, X.; Zhai, T. Strong In-Plane Anisotropic SiP_2 as a IV−V 2D Semiconductor for Polarized Photodetection. *ACS Nano* **2021**, *15* (12), 20442−20452.
(56) Usman, M.; Nisar, S.; Kim, D.-k.; Golovynskyi, S.; Imran, M.; Dastgeer, G.; Wang, L. Polarization-Sensitive Photodetection of Anisotropic 2D Black Arsenic. *J. Phys. Chem. C* **2023**, *127* (19), 9076−9082.

https://doi.org/10.1021/acsami.4c21713
ACS Appl. Mater. Interfaces 2025, 17, 18592−18600